Scripta Materialia 274 (2026) 117157

Contents lists available at ScienceDirect

Scripta Materialia

journal homepage: www.journals.elsevier.com/scripta-materialia

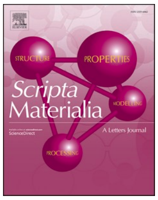

Enhancing hydrogen embrittlement resistance in high-strength martensitic steels via tailoring variant selection at prior austenite grain boundaries

Xiaodong Lan *, Kazuho Okada, Rintaro Ueji, Akinobu Shibata

Research Center for Structural Materials, National Institute for Materials Science, 1-2-1 Sengen, Tsukuba, Ibaraki 305-0047, Japan

ARTICLE INFO

Keywords:
Martensitic steels
Thermomechanical processing
Variant selection
Hydrogen embrittlement
Intergranular fracture

ABSTRACT

This study presents a thermomechanical processing strategy to improve the resistance to hydrogen embrittlement (HE) in martensitic steels through controlling variant selection at prior austenite grain boundaries (PAGBs), while retaining ultrahigh tensile strength (>1.5 GPa). Under identical hydrogen-charging conditions, the 10% hot-compressed specimen exhibited the highest HE resistance, correlating with its largest fraction of low-angle PAGB segments. Misorientation-distribution analysis and tensile tests revealed a non-monotonic dependence of compressive strain: an optimal compressive level maximized the beneficial stress-assisted variant selection at PAGBs, whereas excessive strains promoted self-accommodation of transformation strain in the work-hardened austenite, diminishing the beneficial effect. The improved HE resistance stems from reduced hydrogen trapping, enhanced strain-dissipating slip transfer, and increased cohesive energy at PAGBs. Tailoring variant selection at PAGBs through this simple process thus provides an industry-feasible route to hydrogen-resistant high-strength martensitic steels.

High-strength steels are indispensable in automotive, energy, and infrastructure sectors. The global push for decarbonization and the growing adoption of hydrogen energy have intensified the need for advanced high-strength steels that possess hydrogen embrittlement (HE) resistance, enabling both energy-efficient lightweighting and reliable performance in hydrogen environments [1]. However, these steels are highly susceptible to HE [2,3], and this susceptibility increases with strength—a persistent trade-off that limits their application. Developing engineering strategies that suppress HE without compromising strength is therefore essential.

Lath martensite—a hierarchical microstructure comprising lath, block, packet, and prior austenite grain (PAG)—is characteristic of high-strength low- and medium-carbon steels [4–7]. Although it contains different types of high-angle boundaries, hydrogen-related intergranular (IG) fracture occurs predominantly at prior austenite grain boundaries (PAGBs) [8–11]. This phenomenon is generally attributed to hydrogen segregation at PAGBs [12,13], which lowers cohesive energy and promotes IG decohesion—a brittle failure mode far more severe than quasi-cleavage (QC). Therefore, mitigating IG fracture is paramount for improving the reliability of high-strength martensitic steels in hydrogen-rich environments. Our recent work [14] showed that thermomechanical processing that produces dynamically transformed (DT) ferrite along PAGBs can effectively suppress IG fracture, yet this approach is limited to steels capable of dynamic ferrite transformation. Carbon segregation at PAGBs has also been reported to retard IG fracture, but its effectiveness is confined to low hydrogen levels [15,16]. Recent investigations highlight the potential of tailoring PAGB crystallography to suppress hydrogen-related IG fracture. For example, Archie et al. [17] demonstrated that PAGB segments with low misorientation are more resistant to crack nucleation via micro-cantilever bending tests. Shibata et al. [9,18,19] revealed that low-angle PAGB segments can arrest IG cracks through multiscale three-dimensional analysis. While these findings underscore the role of low-angle PAGB segments in suppressing IG cracking, practical strategies to promote their formation remain lacking.

Furuhara et al. [20–22] reported that specific martensite/bainite variants preferentially nucleated at PAGBs and proposed four variant selection rules, among which the double Kurdjumov–Sachs orientation relationship is most relevant for forming low-angle PAGB segments. Furthermore, studies based on Patel and Cohen's theory indicated that variants accommodating greater external work are preferentially selected under applied stress [23–26]. On the other hand, Kato et al. [27] highlighted the critical role of the applied stress on the primitive transformation process (specifically, the first shear in the

---

* Corresponding author.
E-mail address: LAN.Xiaodong@nims.go.jp (X. Lan).

https://doi.org/10.1016/j.scriptamat.2025.117157
Received 5 October 2025; Received in revised form 16 December 2025; Accepted 26 December 2025

Bogers–Burgers model [28]) in governing variant selection during deformation-induced martensitic transformation. Motivated by these insights, we propose a novel thermomechanical processing strategy that tailors variant selection at PAGBs during martensitic transformation to increase the fraction of low-angle PAGB segments and thereby enhance HE resistance in martensitic steels while retaining ultrahigh tensile strength.

An Fe-5Mn-0.2C alloy (Mn 4.87, C 0.19, S 0.002, O 0.003, N 0.001, Si 0.01, P <0.001, Al 0.01, balance Fe (wt. %)) was used. The elevated Mn content stabilizes austenite and retards dynamic ferrite transformation during hot deformation, enabling a simple study of martensite variant selection. Cylindrical specimens (16 mm diameter × 24 mm height) were machined from the as-received ingot and subjected to thermomechanical processing whose steps are schematically shown in Fig. 1(a). The specimens were austenitized at 900°C for 600 s, then gas-cooled to 600 °C at 15 °C/s. After a 30 s hold for temperature stabilization, they were uniaxially compressed at a strain rate of 0.01 s^{-1} to height reductions of 5 %, 10 %, 20 %, or 30 %, followed by nitrogen gas quenching under maintained compressive loading (i.e., compress and hold at constant displacement) to produce hot-compressed (HC) specimens. These specimens are hereafter designated as 5 %HC, 10 %HC, 20 %HC, and 30 %HC, respectively. As-quenched (AQ) martensite, produced by identical austenitization and immediate quenching without deformation, served as reference. Fig. 1(b) presents the apparent true stress–true strain curves for the specimens compressed at 600°C, assuming uniform deformation and constant volume. Fig. 1(c) shows the load–time curves during compression and subsequent quenching under load; the post-quench load increase is attributed to the volume expansion accompanying martensitic transformation.

The microstructures of the thermo-mechanically processed specimens were characterized by electron backscattering diffraction (EBSD) using a ZEISS Crossbeam 550 L SEM equipped with a Bruker QUANTAX EBSD system. A single-iteration grain dilation cleanup was applied to the EBSD data using a grain tolerance angle of 5°, a minimum grain size of 2 pixels, and a minimum confidence index of 0.2. Micro-tensile specimens (details in [14]) were machined from the thermo-mechanically processed specimens, with the tensile axis perpendicular to the compression axis (CA). The tensile specimens were mechanically polished and cathodically pre-charged with hydrogen at 1 A·m^{-2} for 24 h at room temperature in 3 % NaCl + 3 g·L^{-1} NH$_4$SCN aqueous solution. The susceptibility to HE was evaluated by slow strain rate testing (SSRT, 8.3 × 10^{-6} s^{-1}) at room temperature. Two specimens per condition were tested to ensure reproducibility. Fracture surface morphology was analyzed by SEM. Diffusible hydrogen content (H_D), defined as the cumulative hydrogen amount desorbed from room temperature to 300 °C, was measured by thermal desorption spectroscopy (TDS) using a R-DEC HTDS-004 system at a heating rate of 100 °C·h^{-1}. Both SSRT and TDS were conducted 30 min after hydrogen charging.

Fig. 2 shows the EBSD orientation maps of the AQ, 5 %HC, 10 %HC, 20 %HC, and 30 %HC specimens. The phase maps confirm negligible retained austenite (< 0.2 %) in all specimens. The block, packet, and PAG boundaries were identified through crystallographic variant analysis of EBSD orientation data [4,5]. The average block sizes (equivalent diameter) for the AQ, 5 %HC, 10 %HC, 20 %HC, and 30 %HC specimens are 8.9 μm, 8.4 μm, 7.9 μm, 7.6 μm, and 7.0 μm, respectively. The AQ specimen exhibits the expected hierarchical lath martensite structure, with multiple packets and blocks within equiaxed PAGs. The 5 %HC and 10 %HC specimens retain this hierarchy and show little change in PAG morphology; however, many coarse blocks adhering to PAGBs appear (as indicated in Figs. 2(b–c)), indicating pronounced variant selection. Fewer martensite variants form when variant selection happens, and the selected variants can grow preferentially. Mishiro et al. [24] also observed that the variants preferentially selected under external stress were larger than the average size. At higher reductions, the

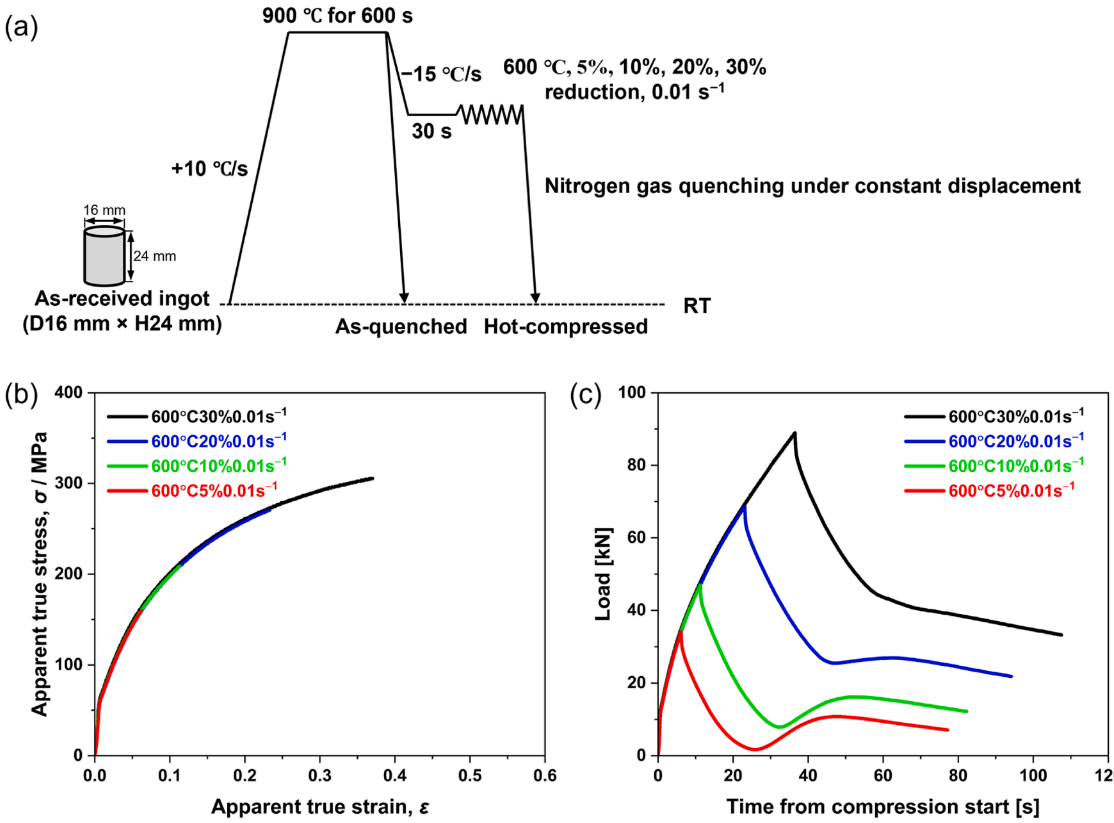

Fig. 1. (a) Thermomechanical processing scheme; (b) Apparent true stress–true strain curves for specimens compressed at 600°C to different reductions; (c) Load–time curves during compression and subsequent nitrogen gas quenching under compressive loading.

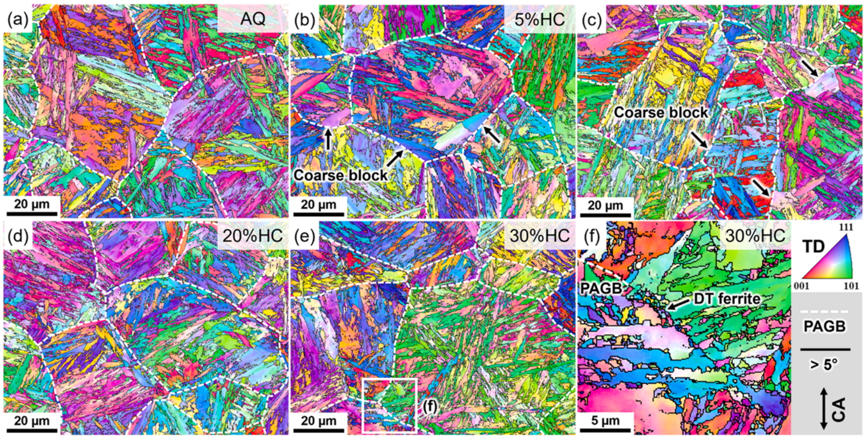

Fig. 2. EBSD orientation maps of the (a) AQ, (b) 5 %HC, (c) 10 %HC, (d) 20 %HC, and (e) 30 %HC specimens; (f) magnified view of the rectangle in (e). Colors in the IPF maps indicate the crystal direction aligned with the specimen's transverse direction (TD), as defined by the stereographic triangle.

microstructure evolves differently. In the 20 %HC specimen, the block-coarsening phenomenon at PAGBs is suppressed; instead, the blocks are refined and the PAGs become slightly elongated. This refinement is more pronounced in the 30 %HC specimen, where the PAGs are more elongated and DT ferrite grains form along the PAGBs (Fig. 2(e)). These ultrafine, equiaxed DT ferrite grains show significantly lower kernel average misorientation than surrounding martensite variants. The transition from block coarsening to refinement reflects two competing effects of hot compression on variant selection. At low strains, compressive stress promotes the preferential nucleation of certain martensite variants, resulting in block coarsening. At higher strains, the work-hardened austenite makes plastic accommodation difficult and thus enhances the necessity for self-accommodation of transformation strain by forming more neighboring variants [29].

As reported, low-angle PAGB segments can arrest IG crack propagation by accommodating crack-tip stress via localized plastic deformation [18,19,30]. Thus, the low-angle PAGB segments fraction can serve as a quantitative measure of the ability to suppress IG fracture. In this study, the misorientation of PAGB segments was measured across three representative PAGs per specimen. Fig. 3(a) schematically illustrates a PAGB and its crystallographic heterogeneity: a segmented boundary of adjoining martensite variants with varying misorientations, rather than a single uniform interface. Figs. 3(b–e) present the misorientation profiles of PAGB segments for the AQ, 5 %HC, 10 %HC, and 20 %HC specimens, with total boundary length (*L*) and segment number (*N*) indicated. The 10 %HC specimen exhibits a significantly higher fraction of low-angle PAGB segments (misorientation$\leq$ 15°) than the AQ, 5 %HC, and 20 %HC specimens. This increase could be attributed to enhanced variant selection at PAGBs. By contrast, variant selection is suppressed in the 20 %HC specimen. These results indicate a non-monotonic dependence of compressive strain: an optimal level maximizes the stress-assisted variant selection at PAGBs, whereas excessive strain suppresses it. Although Σ3 PAGB segments also impede IG cracking [19,30], they are not analyzed in depth here; this study focuses on increasing the fraction of low-angle PAGB segments to enhance the resistance to HE.

Fig. 4(a) shows the H_D for the hydrogen-charged AQ, 5 %HC, 10 %HC, 20 %HC, and 30 %HC specimens. Under identical hydrogen-charging conditions, the H_D first decreased and then increased with increasing hot-compression reduction. The 10 %HC specimen had the lowest H_D despite hot compression introducing lattice defects that trap hydrogen; this is likely because variant selection increased the fraction of low-angle PAGB segments, which would be weaker hydrogen traps [31,32]. At higher strains, the density of hydrogen-trapping sites (e.g., variant boundaries and dislocations) increased, causing H_D to rise. Figs. 4(b–f) present the nominal stress–nominal strain curves for each condition. The tensile strength of uncharged specimens first slightly increased from 1676.75 ± 0.95 MPa (AQ) to 1720.5 ± 12.7 MPa (5 %HC), then decreased to 1579.45 ± 3.95 MPa (10 %HC). Although microstructural refinement and increased dislocation density (AQ → 30 %HC: $3.73 \times 10^{15} \rightarrow 5.82 \times 10^{15}$ m^{-2}; Supplemental Fig. A1) would normally raise the strength, the anomalous strength reduction directly reflects stress-assisted variant selection: a higher fraction of low-angle PAGB segments facilitates slip transfer across PAGBs [33–35] and thus reduces the strength. The tensile strength again rose to 1808.8 ± 18.2 MPa for the 20 %HC specimen due to further refinement, increased dislocation density, and suppression of variant selection at PAGBs. This strengthening trend is only marginally continued in the 30 %HC specimen (1811.8 ± 18.4 MPa), as it is compromised by the softening effect of DT ferrite. Fig. 4(g) summarizes the maximum tensile stress for each condition. Under identical hydrogen-charging conditions, the 10 %HC specimen exhibited the highest load-bearing capacity. To quantify HE susceptibility, we define a hydrogen embrittlement index (HEI) based on the ratio of tensile strength reduction (Fig. 4(h)). The 10 %HC specimen shows the lowest HEI (namely, the highest HE resistance), directly correlating with its largest fraction of low-angle PAGB segments. Notably, the 30 %HC specimen also exhibits superior HE resistance compared with the AQ, 5 %HC, and 20 %HC specimens, attributable to PAGBs being covered by DT ferrite grains [14].

To elucidate the mechanisms underlying the observed HE behavior, fracture surfaces after SSRT were analyzed, as shown in Fig. 5. The uncharged specimens displayed typical ductile fracture features, whereas the hydrogen-charged specimens showed IG and QC features. The hydrogen-charged AQ specimen presented predominantly smooth IG facets with minor QC regions, a morphology typical of martensitic steels failing in the elastic regime. The hydrogen-charged 5 %HC specimen exhibited similar fracture features with some tear ridges on IG facets. In contrast, the 10 %HC specimen showed a reduced area fraction of IG fracture and abundant tear ridges on the macroscopic IG facets (high-magnification images in Supplementary Fig. A2), indicating intense local plasticity before final failure. The hydrogen-charged 20 %HC specimen again exhibited smooth IG facets, which we attributed to suppression of variant selection at PAGBs caused by excessive prior deformation. Finally, although the 30 %HC specimen contained the highest H_D (Fig. 4(a)), it showed a reduced IG area fraction because DT ferrite covered the PAGBs, as reported previously [14].

In this study, martensitic structures with distinct crystallographic and morphological features in PAGB-adhering variants were produced through thermomechanical processing. Figs. 3–5 show a clear correlation between the fraction of low-angle PAGB segments and HE resistance: under identical hydrogen-charging conditions, the 10 %HC specimen, which had the highest fraction of low-angle segments,

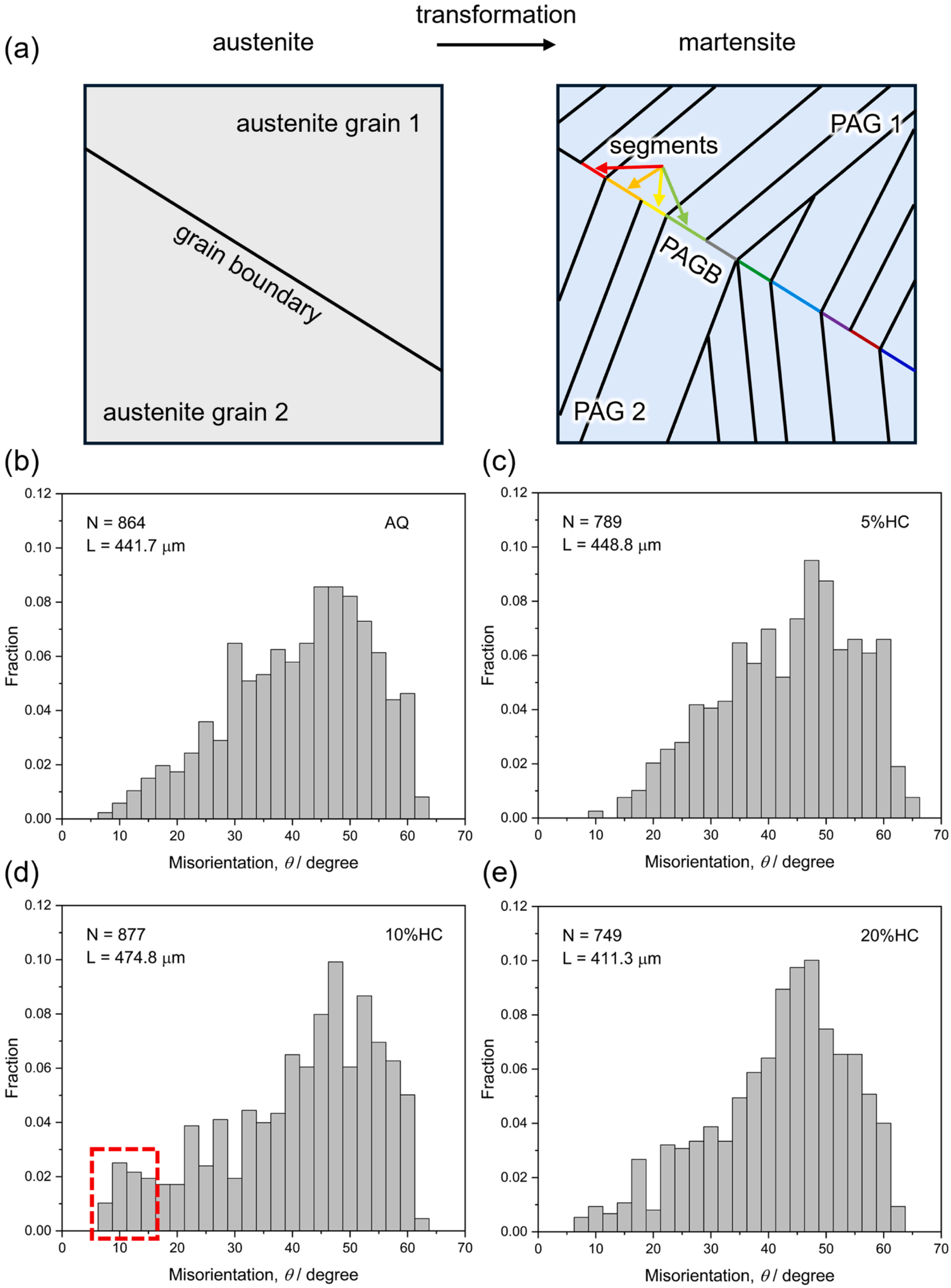

Fig. 3. (a) Schematic of a PAGB; (b–e) Misorientation profiles for the PAGBs in the AQ, 5 %HC, 10 %HC, and 20 %HC specimens.

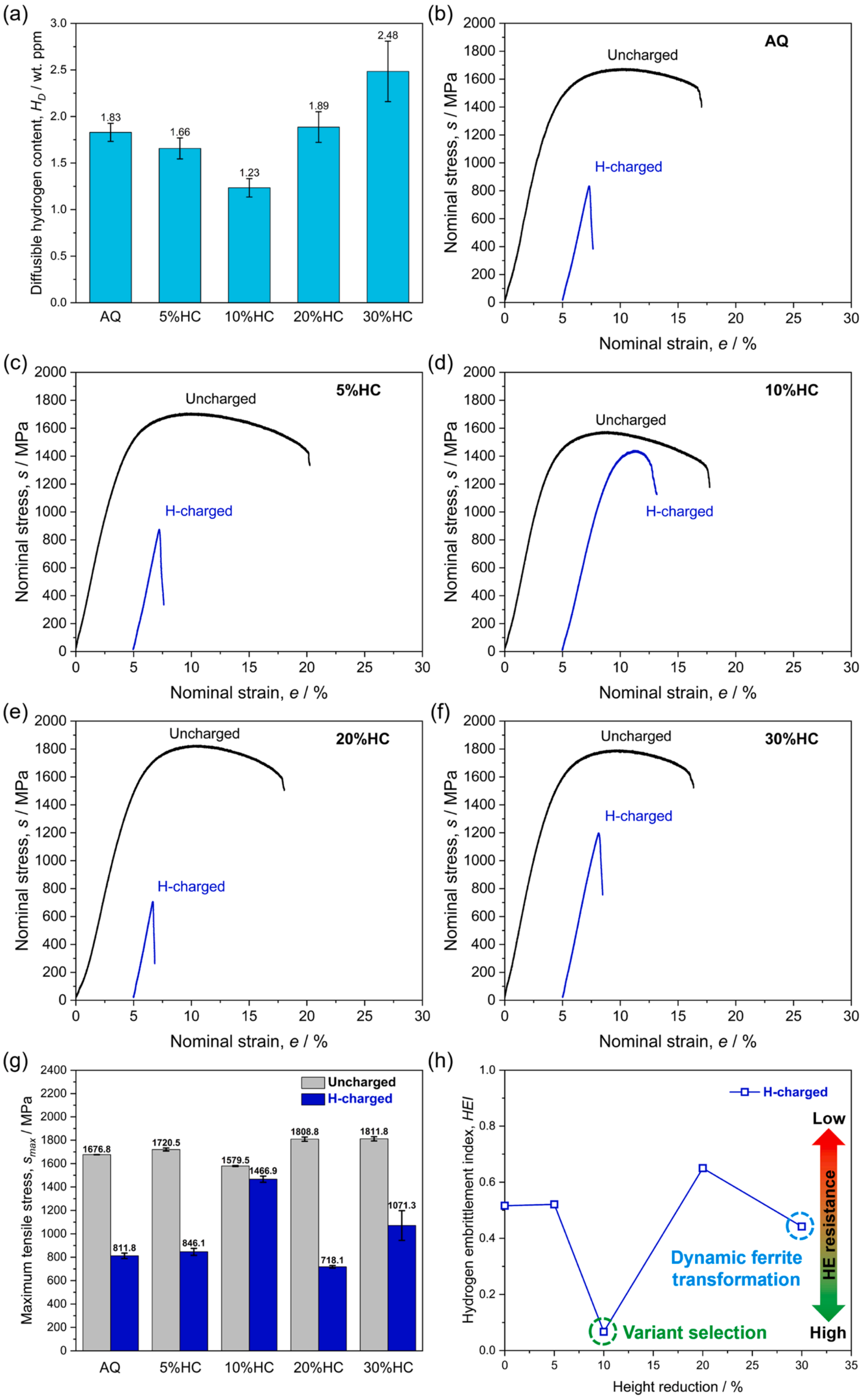

Fig. 4. (a) H_D of the hydrogen-charged AQ, 5 %HC, 10 %HC, 20 %HC, and 30 %HC specimens; (b–f) Nominal stress–nominal strain curves for each condition; (g) Maximum tensile stress for each condition; (h) HEI plotted against hot-compression reductions.

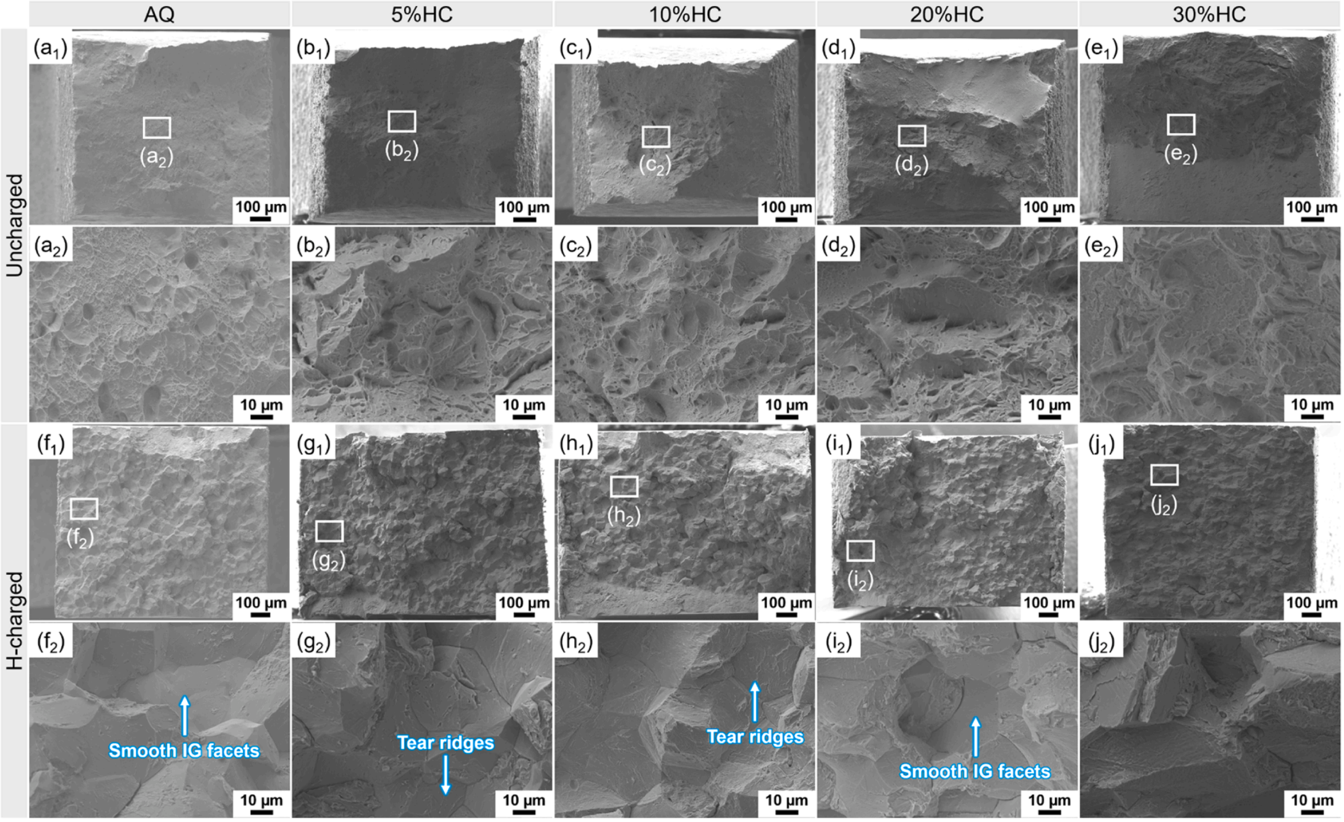

Fig. 5. SEM images of fracture surfaces for (a_1, a_2, f_1, f_2) AQ, (b_1, b_2, g_1, g_2) 5 %HC, (c_1, c_2, h_1, h_2) 10 %HC, (d_1, d_2, i_1, i_2) 20 %HC, and (e_1, e_2, j_1, j_2) 30 %HC specimens. Low-magnification images (a_1–j_1) show overall fracture morphology, while high-magnification images (a_2–j_2) highlight selected areas indicated by rectangles in the corresponding low-magnification images.

exhibited the highest HE resistance while retaining tensile strength above 1.5 GPa. This improvement is attributed to the stress-assisted variant selection at PAGBs during martensitic transformation. The externally applied stress adds a mechanical driving force to the chemical driving force, favoring the nucleation of variants whose transformation strain most effectively relax the applied stress, as formalized by the Patel–Cohen model [23]. Kato et al. [27] further highlighted the critical role of applied stress on the first shear of the Bogers–Burgers model [28] in governing variant selection during deformation-induced martensitic transformation. Furuhara et al. [20] also proposed that the variant for which the maximum component of transformation strain is nearly parallel to the slip direction in the neighboring austenite grain or to the grain boundary plane is preferably formed, and this tendency will be enhanced by externally applied stress. From an energy perspective, forming low-angle PAGB segments under stress is also highly favorable because it minimizes the total energy of the system by reducing boundary energy. Notably, an optimal compressive level maximizes the beneficial variant selection, whereas excessive strain promotes self-accommodation in work-hardened austenite [29], thereby diminishing this effect.

The increased fraction of low-angle PAGB segments is critical for mitigating HE, as their intrinsic characteristics provide multiple synergistic protective mechanisms. First, unlike general high-angle boundaries (except coherent $\Sigma3$ [36]) act as strong hydrogen traps and preferred paths for IG cracking [37,38], low-angle boundaries are consistently reported to be weaker hydrogen traps [31,32] and less susceptible to hydrogen-related IG cracking [9,19,30]. Their lower excess free volume and energy reduce hydrogen trapping potency, as evidenced by the reduced hydrogen absorption capacity in the 10 %HC specimen (Fig. 4(a)) despite hot compression introducing numerous lattice defects. Second, low-angle segments facilitate slip transmission across PAGBs, effectively dissipating strain and mitigating stress concentrations. This is directly reflected in the anomalous decrease in tensile strength observed in the 10 %HC specimen (Fig. 4(d)). Lan et al. [39] reported that strain localization at PAGBs was involved in the sequence of hydrogen-related IG cracking, and Shibata et al. [40] revealed that hydrogen-related IG fracture originated from stress-controlled decohesion, both of which emphasize the detrimental role of local stress/strain concentrations in IG cracking. Third, the high coherency and strong atomic bonding of low-angle PAGB segments intrinsically resist hydrogen-related IG crack initiation/propagation. This is supported by the presence of abundant tear ridges on the IG facets of the hydrogen-charged 10 %HC specimen (Fig. 5(h_2)), which indicates intense local plasticity prior to failure rather than brittle boundary decohesion. The density functional theory calculations by Matsumoto et al. [41] also suggested that hydrogen causes a greater reduction in cohesive energy at higher-energy (high-angle) grain boundaries. Follow-up work will statistically analyze variant selection mechanisms and investigate how variant selection influences strain localization, hydrogen trapping, and crack initiation/propagation to develop a systematic, in-depth mechanistic understanding.

To summarize, we developed a novel thermomechanical processing strategy that controls variant selection at PAGBs to enhance HE resistance in martensitic steels while retaining ultrahigh tensile strength (>1.5 GPa). Under identical hydrogen-charging conditions, the 10 %HC specimen showed the highest HE resistance, correlating with its largest fraction of low-angle PAGB segments. Misorientation-distribution analysis and SSRT revealed a non-monotonic dependence of compressive strain: an optimal level maximizes the beneficial stress-assisted variant selection at PAGBs, whereas excessive strain promotes self-accommodation in work-hardened austenite, diminishing the beneficial effect. The enhanced HE resistance stems from the increased fraction of low-angle PAGB segments, which reduces hydrogen trapping at PAGBs, facilitates strain-dissipating slip transfer across PAGBs, and increases boundary cohesive energy. These findings establish tailoring variant selection at PAGBs via thermomechanical processing as an industry-implementable strategy for producing hydrogen-resistant high-strength martensitic steels.

CRediT authorship contribution statement

Xiaodong Lan: Writing – review & editing, Writing – original draft, Validation, Methodology, Investigation, Formal analysis, Data curation, Conceptualization. **Kazuho Okada:** Writing – review & editing, Funding acquisition. **Rintaro Ueji:** Writing – review & editing, Resources, Methodology. **Akinobu Shibata:** Writing – review & editing, Validation, Supervision, Resources, Project administration, Methodology, Funding acquisition, Conceptualization.

Declaration of competing interest

The authors declare that they have no known competing financial interests or personal relationships that could have appeared to influence the work reported in this paper.

Acknowledgements

This work was financially supported by JSPS KAKENHI (Grant Numbers JP22K18910, JP23H01717, JP23K13541, and JP24K01221) and MEXT Program: Data Creation and Utilization Type Material Research and Development Project Grant Number JPMXP1122684766.

Supplementary materials

Supplementary material associated with this article can be found, in the online version, at doi:10.1016/j.scriptamat.2025.117157.

References

[1] D. Raabe, C.C. Tasan, E.A. Olivetti, Strategies for improving the sustainability of structural metals, Nature 575 (7781) (2019) 64–74.

[2] J. Venezuela, Q. Liu, M. Zhang, Q. Zhou, A. Atrens, A review of hydrogen embrittlement of martensitic advanced high-strength steels, Corros. Rev. 34 (3) (2016) 153–186.

[3] M.L. Martin, M.J. Connolly, F.W. DelRio, A.J. Slifka, Hydrogen embrittlement in ferritic steels, Appl. Phys. Rev. 7 (4) (2020) 041301.

[4] S. Morito, H. Tanaka, R. Konishi, T. Furuhara, T. Maki, The morphology and crystallography of lath martensite in Fe-C alloys, Acta Mater 51 (6) (2003) 1789–1799.

[5] S. Morito, X. Huang, T. Furuhara, T. Maki, N. Hansen, The morphology and crystallography of lath martensite in alloy steels, Acta Mater 54 (19) (2006) 5323–5331.

[6] H. Kitahara, R. Ueji, N. Tsuji, Y. Minamino, Crystallographic features of lath martensite in low-carbon steel, Acta Mater 54 (5) (2006) 1279–1288.

[7] A. Shibata, G. Miyamoto, S. Morito, A. Nakamura, T. Moronaga, H. Kitano, I. Gutierrez-Urrutia, T. Hara, K. Tsuzaki, Substructure and crystallography of lath martensite in as-quenched interstitial-free steel and low-carbon steel, Acta Mater 246 (2023) 118675. -118675.

[8] M. Wang, E. Akiyama, K. Tsuzaki, Hydrogen degradation of a boron-bearing steel with 1050 and 1300MPa strength levels, Scr. Mater. 52 (5) (2005) 403–408.

[9] A. Shibata, I. Gutierrez-Urrutia, A. Nakamura, K. Okada, G. Miyamoto, Y. Madi, J. Besson, T. Hara, K. Tsuzaki, Three-dimensional propagation behavior of hydrogen-related intergranular cracks in high-strength martensitic steel, Int. J. Hydrogen Energy 48 (88) (2023) 34565–34574.

[10] Y. Momotani, A. Shibata, N. Tsuji, Hydrogen embrittlement behaviors at different deformation temperatures in as-quenched low-carbon martensitic steel, Int. J. Hydrogen Energy 47 (5) (2022) 3131–3140.

[11] C.J. McMahon, Hydrogen-induced intergranular fracture of steels, Eng. Fract. Mech. 68 (6) (2001) 773–788.

[12] Y. Momotani, A. Shibata, D. Terada, N. Tsuji, Effect of strain rate on hydrogen embrittlement in low-carbon martensitic steel, Int. J. Hydrogen Energy 42 (5) (2017) 3371–3379.

[13] Y. Momotani, A. Shibata, T. Yonemura, Y. Bai, N. Tsuji, Effect of initial dislocation density on hydrogen accumulation behavior in martensitic steel, Scr. Mater. 178 (2020) 318–323.

[14] X. Lan, K. Okada, R. Ueji, A. Shibata, Improving hydrogen embrittlement resistance in high-strength martensitic steels via thermomechanical processing, Scr. Mater. 264 (2025) 116711.

[15] K. Okada, A. Shibata, T. Sasaki, H. Matsumiya, K. Hono, N. Tsuji, Improvement of resistance against hydrogen embrittlement by controlling carbon segregation at prior austenite grain boundary in 3Mn-0.2C martensitic steels, Scr. Mater. 224 (2023) 115043. -115043.

[16] K. Okada, A. Shibata, Y. Kimura, M. Yamaguchi, K.I. Ebihara, N. Tsuji, Effect of carbon segregation at prior austenite grain boundary on hydrogen-related crack propagation behavior in 3Mn-0.2C martensitic steels, Acta Mater 280 (2024) 120288.

[17] F. Archie, S. Zaefferer, On variant selection at the prior austenite grain boundaries in lath martensite and relevant micro-mechanical implications, Mater. Sci. Eng., A 731 (2018) 539–550.

[18] A. Shibata, I. Gutierrez-Urrutia, A. Nakamura, G. Miyamoto, Y. Madi, J. Besson, T. Hara, K. Tsuzaki, Multi-scale three-dimensional analysis on local arrestability of intergranular crack in high-strength martensitic steel, Acta Mater 234 (2022) 118053. -118053.

[19] A. Shibata, I. Gutierrez-Urrutia, A. Nakamura, T. Moronaga, K. Okada, Y. Madi, J. Besson, T. Hara, Local crack arrestability and deformation microstructure evolution of hydrogen-related fracture in martensitic steel, Corros. Sci. 233 (2024) 112092.

[20] T. Furuhara, H. Kawata, S. Morito, G. Miyamoto, T. Maki, Variant selection in grain boundary nucleation of upper bainite, Metall. Mater. Trans. A 39 (5) (2008) 1003–1013.

[21] T. Kaneshita, G. Miyamoto, T. Furuhara, Variant selection in grain boundary nucleation of bainite in Fe-2Mn-C alloys, Acta Mater 127 (2017) 368–378.

[22] J.H. Kim, G. Miyamoto, A. Shibata, T. Hojo, M. Koyama, Y. Zhang, T. Furuhara, Influence of austenite grain boundary misorientation on hydrogen-induced intergranular crack propagation in a medium carbon martensitic steel, Acta Mater 274 (2024) 120036.

[23] J.R. Patel, M. Cohen, Criterion for the action of applied stress in the martensitic transformation, Acta Metall 1 (5) (1953) 531–538.

[24] Y. Mishiro, S. Nambu, J. Inoue, T. Koseki, Effect of stress on variant selection in lath martensite in low-carbon steel, ISIJ Int 53 (8) (2013) 1453–1461.

[25] S. Kundu, H.K.D.H. Bhadeshia, Transformation texture in deformed stainless steel, Scr. Mater. 55 (9) (2006) 779–781.

[26] S. Kumar, N.N. Pai, S. Manda, U. Tewary, D.T. Fullwood, S.K. Giri, S. Kundu, S.V.S. N. Murty, C.R. Anoop, I. Samajdar, Austenite residual stress and lath martensite variant selection in low carbon steels, Acta Mater 289 (2025) 120885.

[27] M. Kato, T. Mori, Stress-induced martensite in single crystals of an Fe-23Ni-5Cr alloy, Acta Metall 24 (9) (1976) 853–860.

[28] A.J. Bogers, W.G. Burgers, Partial dislocations on the {110} planes in the B.C.C. lattice and the transition of the F.C.C. into the B.C.C. lattice, Acta Metall 12 (2) (1964) 255–261.

[29] H. Kawata, K. Sakamoto, T. Moritani, S. Morito, T. Furuhara, T. Maki, Crystallography of ausformed upper bainite structure in Fe–9Ni–C alloys, Mater. Sci. Eng. 438-440 (2006) 140–144. A.

[30] T. Chen, M. Koyama, T. Chiba, E. Akiyama, K. Takai, Mesoscale quantification of grain boundary character and local plasticity in hydrogen-assisted intergranular and intergranular-like cracking paths in tempered martensitic steel, Mater. Sci. Eng., A 886 (2023) 145718.

[31] R. Sato, K. Takai, Quantitative hydrogen trap states on high-angle grain boundaries and at dislocations in iron, Scr. Mater. 228 (2023) 115339.

[32] S. Jothi, T.N. Croft, S.G.R. Brown, Influence of grain boundary misorientation on hydrogen embrittlement in bi-crystal nickel, Int. J. Hydrogen Energy 39 (35) (2014) 20671–20688.

[33] R. Alizadeh, M. Peña-Ortega, T.R. Bieler, J. Llorca, A criterion for slip transfer at grain boundaries in Al, Scr. Mater. 178 (2020) 408–412.

[34] T.R. Bieler, R. Alizadeh, M. Peña-Ortega, J. Llorca, An analysis of (the lack of) slip transfer between near-cube oriented grains in pure Al, Int. J. Plast. 118 (2019) 269–290.

[35] K. Okada, Y. Watase, M. Park, K. Tsuzaki, A. Shibata, Origin of the trade-off relationship between tensile strength and hydrogen embrittlement resistance, Acta Mater 303 (2026) 121683.

[36] Y. He, Y. Su, H. Yu, C. Chen, First-principles study of hydrogen trapping and diffusion at grain boundaries in γ-Fe, Int. J. Hydrogen Energy 46 (10) (2021) 7589–7600.

[37] R. Latypova, O. Seppälä, T. Tun Nyo, T. Kauppi, S. Mehtonen, H. Hänninen, J. Kömi, S. Pallaspuro, Influence of prior austenite grain structure on hydrogen-induced fracture in as-quenched martensitic steels, Eng. Fract. Mech. 281 (2023) 109090.

[38] Y.-S. Chen, H. Lu, J. Liang, A. Rosenthal, H. Liu, G. Sneddon, I. McCarroll, Z. Zhao, W. Li, A. Guo, J.M. Cairney, Observation of hydrogen trapping at dislocations, grain boundaries, and precipitates, Science 367 (6474) (2020) 171–175.

[39] X. Lan, K. Okada, I. Gutierrez-Urrutia, A. Shibata, Quantitative analysis of local plasticity accompanying hydrogen-related fracture in low-carbon martensitic steel, Int. J. Hydrogen Energy 50 (2024) 333–341.

[40] A. Shibata, T. Yonemura, Y. Momotani, M. Park, S. Takagi, Y. Madi, J. Besson, N. Tsuji, Effects of local stress, strain, and hydrogen content on hydrogen-related fracture behavior in low-carbon martensitic steel, Acta Mater 210 (2021) 116828. -116828.

[41] R. Matsumoto, M. Riku, N. Miyazaki, S. Taketomi, Hydrogen-grain boundary interaction in Fe, Fe-C, and Fe-N systems, Prog. Nucl. Sci. Technol. 2 (2011) 9–15.